logs had binding affinities similar to those of the RNA oligonucleotides (Table 1), consistent with the notion that 2′-O-methyl:RNA hybrids have affinities and geometries similar to RNA:RNA duplexes (*16*). The binding affinity of 2′-O-methyl phosphorothioate oligonucleotides for TAR was approximately ten times lower than that of 2′-O-methyl phosphodiesters. DNA and phosphorothioate analogs showed no detectable binding to the 12-base oligonucleotides and very slight binding to the 17-base oligonucleotides. This may be because the structure of DNA:RNA hybrids is different from that of RNA:RNA duplexes and because pseudo–half-knotting geometries appropriate for A-form helices are not optimal for DNA:RNA complexes. In addition, 2′-deoxyoligonucleotides hybridize to RNA much less tightly than do RNA (*17*) or 2′-O-methyl analogs.

Although considerable efforts are being directed at targeting RNA for therapeutic purposes, target site selection is still largely an empirical process. Analysis of the RNA target structure and bound complex stability and structure can assist in the design and optimization of functional antisense oligonucleotides (*18, 19*). By selection of relatively simple, short RNA structures, such as hairpin loops, and by binding with appropriately designed oligonucleotides, stable pseudo–half-knot structures can be formed.

Knowledge of the structure of a drug-target complex can also facilitate additional improvement in drug design. For example, results of the OP•Cu experiment could be used to design oligonucleotides to specifically cleave TAR near C-19. Moreover, these data demonstrate approaches to create nuclease-stable oligonucleotides that bind RNA with high affinity.

## REFERENCES


1. Y. Eguchi, T. Itoh, J. Tomizawa, *Annu. Rev. Biochem.* **60**, 631 (1991).
2. G. W. Witherell, H.-N. Wu, O. C. Uhlenbeck, *Biochemistry* **29**, 11051 (1990).
3. J. L. Casey *et al.*, *Science* **240**, 924 (1988).
4. M. Junker-Niepmann, R. Bartenschlager, H. Schaller, *EMBO J.* **9**, 3389 (1990).
5. C. A. Rosen, G. N. Pavlakis, *AIDS* **4**, 499 (1990).
6. C. W. A. Pleij, *Trends Biochem. Sci.* **15**, 143 (1990).
7. C. W. Pleij and L. Bosch, *Methods Enzymol.* **180**, 289 (1989).
8. J. D. Puglisi, J. R. Wyatt, I. Tinoco, Jr., *Acc. Chem. Res.* **24**, 152 (1991).
9. C. W. Pleij, K. Rietveld, L. Bosch, *Nucleic Acids Res.* **13**, 1717 (1985).
10. S. Roy, U. Delling, C.-H. Chen, C. A. Rosen, N. Sonenberg, *Genes Dev.* **4**, 1365 (1990).
11. C. Dingwall *et al.*, *Proc. Natl. Acad. Sci. U.S.A.* **86**, 6925 (1989).
12. D. J. Ecker, unpublished material.
13. C. B. Chen and D. S. Sigman, *J. Am. Chem. Soc.* **110**, 6570 (1988).
14. K. M. Weeks, C. Ampe, S. C. Schultz, T. A. Steitz, D. M. Crothers, *Science* **249**, 1281 (1990).
15. A. M. Pyle, J. A. McSwiggen, T. R. Cech, *Proc. Natl. Acad. Sci. U.S.A.* **87**, 8187 (1990).
16. H. Inoue *et al.*, *Nucleic Acids Res.* **15**, 6131 (1987).
17. K. B. Hall and L. W. McLaughlin, *Biochemistry* **30**, 10606 (1991).
18. D. Ecker, in *Antisense Research and Applications*, S. Crooke and B. Lebleu, Eds., in preparation.
19. S. T. Crooke, *Annu. Rev. Pharmacol. Toxicol.* **32**, 329 (1992).



20. The authors acknowledge D. Sigman for the gift of 5-iodoacetamido-1,10-phenanthroline; R. Cedergren for the RNase program; I. Tinoco for introducing us to pseudoknots; and S. Crooke, J. Wyatt, O. Uhlenbeck, and I. Tinoco for helpful discussions and for critically reviewing this manuscript.


# Combining Experimental Information from Crystal and Solution Studies: Joint X-ray and NMR Refinement


Boaz Shaanan,* Angela M. Gronenborn, Gerson H. Cohen, Gary L. Gilliland, B. Veerapandian, David R. Davies, G. Marius Clore



**Joint refinement of macromolecules against crystallographic and nuclear magnetic resonance (NMR) observations is presented as a way of combining experimental information from the two methods. The model of interleukin-1β derived by the joint x-ray and NMR refinement is shown to be consistent with the experimental observations of both methods and to have crystallographic *R* value and geometrical parameters that are of the same quality as or better than those of models obtained by conventional crystallographic studies. The few NMR observations that are violated by the model serve as an indicator for genuine differences between the crystal and solution structures. The joint x-ray–NMR refinement can resolve structural ambiguities encountered in studies of multidomain proteins, in which low- to medium-resolution diffraction data can be complemented by higher resolution NMR data obtained for the individual domains.**


With the emergence of NMR as a technique for determining the three-dimensional structure of proteins alongside crystallography (*1*), combination of experimental data from both methods opens a new avenue for the elucidation of macromolecular structures. A potential major hurdle in implementing such an approach, however, has been the apparent discrepancy between models derived by the two methods. Typically, the root-mean-square (rms) differences between backbone atoms of structures determined by the two methods are ~1.0 Å, with local differences of up to 2.0 Å or more (*2, 3*). Moreover, models obtained from crystallographic studies are frequently incompatible with the NMR data, as manifested in a relatively large number of nuclear Overhauser effect (NOE) violations; conversely, models obtained by NMR procedures tend to fit the x-ray data poorly (*R* values of 0.40 to 0.50). In this report we present a joint x-ray–NMR refinement and demonstrate that crystallographic and NMR data can be combined to produce models that are compatible with both experimental methods in that they have a minimal number of NOE violations and *R* values comparable to those derived from refinement against the crystallographic data alone. Further, the residual NOE violations in the combined model can serve as a reliable measure of genuine differences between the solution and crystal structures. A likely application of the method would be, for example, in the determination of structures of multidomain proteins.

The discrepancies between models derived from crystallographic and NMR methods are generally ascribed to distortions caused by crystal forces and differences in the media in which the two experiments are performed (*2, 3*). However, because both methods produce models through procedures that aim to satisfy the experimental data available to each technique and, at the same time, sets of stereochemical restraints (*4, 5*), the differences between the models may equally well be a reflection of inconsistencies between the computational procedures rather than that of genuine variations emanating from different molecular environments in the two experiments. The X-PLOR suite (*6*) provides a natural framework for testing this hypothesis. The structure selected as a test case was that of interleukin-1β (IL-1β), for which high-resolution NMR (*7*) and crystal structures (*8–10*) have been reported.


B. Shaanan, A. M. Gronenborn, G. H. Cohen, D. R. Davies, G. M. Clore, Laboratories of Molecular Biology and Chemical Physics, National Institute of Diabetes and Digestive and Kidney Diseases, National Institutes of Health, Building 2, Bethesda, MD 20892.
G. L. Gilliland and B. Veerapandian, Center for Advanced Research in Biotechnology of the Maryland Biotechnology Institute, University of Maryland, Shady Grove, and the National Institute of Standards and Technology, Rockville, MD 20850.

*Present address: Department of Biological Chemistry, The Hebrew University of Jerusalem, Jerusalem 91904, Israel.

The restrained minimized mean NMR model [entry 6I1B in the Brookhaven Protein Data Bank (PDB); the model includes six water molecules (*7*)] was rotated and translated in the unit cell to fit the crystallographic model of Veerapandian *et al.* [entry 4I1B in the PDB (*10*)]. This model was subjected to several rounds of joint simulated annealing refinement (*11*) against the NMR data and the x-ray observations. The weights on the observations were increased gradually during 200 steps of the simulated annealing at 3000 K until the weights on the x-ray terms were identical to those that would be used in the absence of NMR observations, and the weights on the NMR observations were one-half of their values in the NMR work on IL-1β (*7*). Such gradual increase of weights ensures convergence of the simulated annealing process to a global minimum region (*12*). In the final stages of the refinement, the weights on the NMR observations were those used in the NMR structure determination reported in (*7*). Selection of the appropriate relative weights between the experimental observations and the stereochemical restraints has been an intricate aspect of restrained refinement procedures (*4, 5, 13*) and is further complicated in the case of joint refinement (*14*), in which observations from two different techniques are involved. The net effect of the weighting scheme applied in this work was a refinement process dominated by the x-ray target function with the NMR observations and their linked target function serving as an extra set of restraints. Such a scheme guarantees convergence to a low crystallographic *R* value even in cases in which the differences between the solution and crystal structure are large (see below). The agreement between the model thus produced and the x-ray data was at least as good as the agreement achieved in the crystallographic studies of IL-1β (*8–10*) or in the refinement in the absence of NOEs (*11*), while the number of torsion angle and NOE violations was very small (Table 1). Alternative schemes, in which higher weights were given to the NMR observations, led to unacceptably high crystallographic *R* values. Interestingly, the free *R* value (*13*) of the model JR derived by the joint x-ray–NMR refinement (0.254) is somewhat lower than that obtained for the 4I1B model (0.286), which was refined against x-ray data only (*11*), suggesting that the phases calculated from the JR model are more accurate than those derived from the 4I1B model. However, the significance of such a small difference in the free *R* values is difficult to assess until the ability of this new measure to discriminate between the phasing accuracy of similar atomic models is established.

The Cα trace of the model obtained

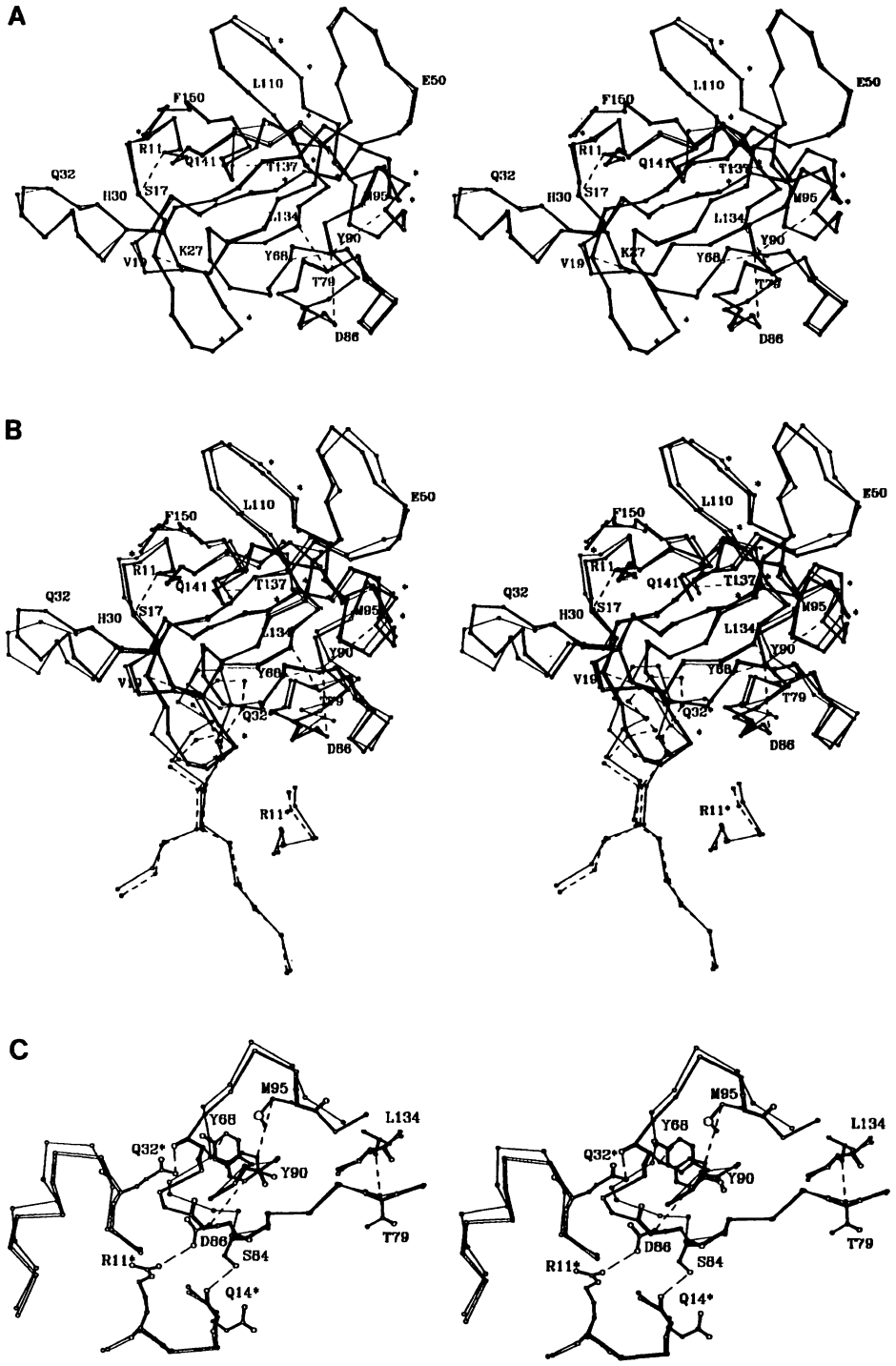


**Fig. 1.** Comparison between the IL-1β model after joint refinement (model JR, full bonds), the NMR model (6I1B, single bonds), and the crystallographic (4I1B, single bonds) model (stereo). The residual NOE violations after the joint refinement are marked by asterisks for internal and sequential violations and dashed lines for long-range violations. Specific residues are marked by the single-letter code (*18*) followed by a number, with asterisks for symmetry-related residues (stereo). (**A**) Superposition of model JR and 4I1B. (**B**) Superposition of model JR and the NMR model 6I1B with residues 10 to 15 and 25 to 45 from the symmetry-related molecule, which interact in the crystal with residues around $Tyr^{90}$ (single bonds for model JR and dashed bonds for model 6I1B); (**C**) A detailed view of the interactions in the crystal between residues around $Tyr^{90}$ and residues in the loop 31 to 36. Residues from model JR (double bonds in the symmetry-related molecule) are superimposed on residues from the NMR model 6I1B (single bonds in the symmetry-related molecule). Long-range NOE violations are marked by short dashes and hydrogen bonds and the salt bridge are marked by long dashes. Note that residues 31 to 36 are shifted in the crystal without causing any NOE violations, whereas the shift of residues 79 to 97 entails such violations in model JR.

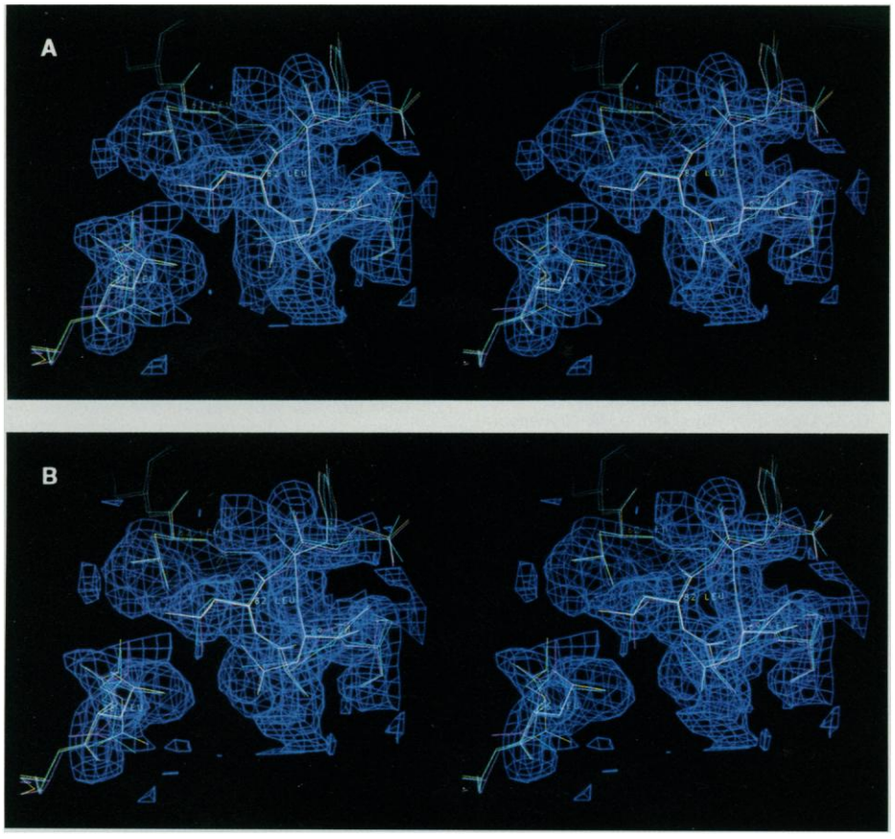


**Fig. 2.** Omit maps (*19*) of the region around Leu$^{69}$ and Leu$^{82}$ (stereo). Maps are calculated at 1$\sigma$ level, with the JR (yellow), NONOE (red), and 4I1B (green) models superimposed. (**A**) Map calculated with phases derived from the model JR (*11*). Note the clear indication for an alternative conformation for Leu$^{82}$. Identical indication was found in a simulated-annealing–omit map, which was obtained by further simulated-annealing refinement at 1000 K of the JR model against the x-ray and NMR data omitting Leu$^{82}$ and neighboring atoms within a 5 Å radius. (**B**) Map calculated with phases derived from model 4I1B (*10*).

**Table 1.** Agreement of IL-1β models with crystallographic and NMR observations.

| Model | JR* | NONOE† | 4I1B‡ | 6I1B§ |
|---|---|---|---|---|
| *R* value | 0.214 | 0.216 | 0.229‖ | 0.45 |
| Rms deviation from ideality | | | | |
| Bond length (Å) | 0.006 | 0.007 | 0.018 | 0.005 |
| Bond angles (degrees) | 2.2 | 2.9 | 3.5 | 2.1 |
| NOE violations | | | | |
| Distance restraints¶ | 17/0/0 | 63/28/1 | 54/24/12 | 0/0/0 |
| Dihedral restraints (>10°) | | | | |
| φ | 0 | 2 | 2 | 0 |
| ψ | 0 | 4 | 1 | 0 |
| $\chi_1$ | 2 | 25 | 19 | 0 |

*Model produced by joint x-ray–NMR refinement (*11*). †Model produced by conventional simulated annealing refinement of the restrained minimized mean NMR structure 6I1B (*7*) against the x-ray data and without NMR restraints (*11*). ‡X-ray structure described in (*10*). §Restrained minimized mean NMR structure described in (*7*). ‖Water molecules observed in the crystal were excluded. ¶Values are restraints from 0.5 to 1.0 Å, 1.0 to 2.0 Å, and greater than 2.0 Å.

**Table 2.** Positonal rms differences between IL-1β models. The notation of the models is as follows: 4I1B is the crystal structure reported in (*10*); 6I1B is the restrained minimized mean NMR structure reported in (*7*); JR is the joint x-ray–NMR structure reported in this work (*11*); NONOE is the model produced by conventional simulated annealing refinement of 6I1B against the x-ray data alone (*11*).

| Models | Residues 3 to 151 (Å) | | Internal residues* (Å) | |
|---|---|---|---|---|
| | Backbone | All atoms | Backbone | All atoms |
| JR/4I1B | 0.39 | 1.05 | 0.20 | 0.61 |
| JR/NONOE | 0.30 | 1.07 | 0.17 | 0.48 |
| JR/6I1B | 0.83 | 1.46 | 0.67 | 0.93 |
| 4I1B/NONOE | 0.39 | 1.14 | 0.23 | 0.66 |
| 4I1B/6I1B | 0.87 | 1.48 | 0.70 | 1.01 |
| 6I1B/NONOE | 0.85 | 1.43 | 0.69 | 0.99 |

*Residues for which the surface accessibility is ≤40% of the same residue in an extended Gly-X-Gly tripeptide segment (*17*).

from the joint x-ray–NMR refinement is indistinguishable in most places from the model 4I1B that was derived solely from crystallographic information (*10*) (Fig. 1A and Table 2), with the exception of one region of large apparent discrepancy reflecting differences in interpretation of the electron density map in the ill-defined segment around Gly$^{139}$-Gly$^{140}$ [this segment has a different conformation in each of the four independent studies (*7–10*)]. Superposition of the NMR model 6I1B (*7*) on the JR model, on the other hand (Fig. 1B), clearly delineates regions with differences up to 4 Å between the two models. Surprisingly, the number of residual NOE violations above 0.5 Å in the joint refinement model is only 17, compared to much higher numbers in the crystallographic and NONOE models [Table 1 (*3*)], with most of the long-range violations concentrated in one region of the IL-1β structure around Tyr$^{90}$ (Fig. 1B). This region, and the region around residues 31 to 36, are the ones that differ most between the independent NMR model 6I1B and the crystallographic model 4I1B (*3*). However, there are no residual NOE violations around residues 31 to 36 despite the large shift in their backbone conformation under the effect of the x-ray data during the joint refinement. A closer look at these two regions (Fig. 1C) reveals that in the crystal the polypeptide around Tyr$^{90}$ interacts through a series of hydrogen bonds (Oγ Ser$^{84}$–O Gln$^{14}$ and O Tyr$^{90}$–Nε2 Gln$^{32}$) and a salt bridge (Oδ2 Asp$^{86}$–Nη2 Arg$^{11}$) with the chain of a symmetry-related molecule encompassing residues 31 to 36. In the crystal as shown by the joint x-ray–NMR refinement, the 31 to 36 loop moves away from its position in the NMR model without violating the observed NOEs, probably because of its inherent flexibility, as judged by the relatively high temperature factors of the residues in this region (average *B* of 51 Å$^2$ for backbone atoms compared to 33 Å$^2$ for the whole structure). However, the structure around Tyr$^{90}$ is more rigid (average *B* of 31 Å$^2$). As it is moved away from the position it occupies in the NMR model, its conformation is distorted, resulting in several NOE viola-

tions. Thus the difference between the region around $Tyr^{90}$ in the NMR model and the crystallographic studies reflects a genuine difference between the solution and the crystal conformation. The differences around the loop encompassing residues 31 to 36, however, although arising from crystal interactions, are misleading, because as shown by the joint x-ray–NMR refinement and the concomitant lack of NOE violations, the crystallographic model is consistent with the NMR observations (*15*).

An attractive aspect of the joint x-ray–NMR refinement method is a decreased necessity for human intervention in rebuilding the model throughout the process. Because the NMR observations ensure maintenance of proper local interactions between side chains, they can assist in selecting side chain conformations during interpretation of the electron density map, as demonstrated for example in the case of $Leu^{69}$ and $Leu^{82}$. Several NOE interactions between the side chain protons of these two residues and protons of the adjacent $Leu^{26}$ and $Leu^{80}$, as well as dihedral NMR restraints on the $\chi_1$ angles, lock their side chains in a conformation that is different from the one observed in the refinements without NOE restraints (models 4I1B and NONOE). The resulting electron density map confirms the choice of conformation for both $Leu^{69}$ and $Leu^{82}$ (Fig. 2). Unlike the maps produced by the refinements without NOEs (Fig. 2B), it also indicates that alternative conformations are possible, particularly for $Leu^{82}$ (Fig. 2A). Such amplification of the information contained in the diffraction data, together with the improvement in the ratio of parameters to observations, suggest that incorporation of the NMR observations, where available, has the potential of improving the convergence of crystallographic refinement procedures.

Although previous studies have shown that structures determined by NMR can be used as initial models for solving crystal structures by the molecular replacement method (*16*), the present study opens the way for a full amalgamation of the NMR and x-ray data throughout the structure determination process. A typical situation in which the diffraction data can be complemented by the NMR observations is in studies of multidomain proteins, for which only the overall structure can be modeled reliably from medium to low-resolution electron density maps, but more detailed models of the individual domains can be obtained from NMR data pertaining to higher resolution.

## REFERENCES AND NOTES


1. K. Wüthrich, *Science* **243**, 45 (1989); G. M. Clore and A. M. Gronenborn, *ibid.* **252**, 1390 (1991).
2. M. Billeter *et al.*, *J. Mol. Biol.* **206**, 677 (1989); T. A. Holak *et al.*, *ibid.* **210**, 649 (1989); G. M. Clore and A. M. Gronenborn, *ibid.* **217**, 611 (1991); in *Computational Aspects of the Study of Biological Macromolecules by NMR Spectroscopy*, J. C. Hoch *et al.*, Eds. (Plenum, New York, 1991), pp. 57–65.
3. G. M. Clore and A. M. Gronenborn, *J. Mol. Biol.* **221**, 47 (1991).
4. A. Jack and M. Levitt, *Acta Crystallogr.* **A34**, 931 (1978).
5. W. A. Hendrickson and J. H. Konnert, in *Computing in Crystallography*, R. Diamond, S. Ramaseshan, K. Venkatesan, Eds. (Indian Academy of Sciences, Bangalore, 1980), pp. 13.01–13.23.
6. A. T. Brünger, G. M. Clore, A. M. Gronenborn, M. Karplus, *Proc. Natl. Acad. Sci. U.S.A.* **83**, 3801 (1986); A. T. Brünger, J. Kuriyan, M. Karplus, *Science* **235**, 458 (1987); A. T. Brünger, G. M. Clore, A. M. Gronenborn, M. Karplus, *Protein Eng.* **1**, 399 (1987); A. T. Brünger, *X-PLOR, Version 2.1* (Yale University, New Haven, CT, 1990).
7. G. M. Clore, P. T. Wingfield, A. M. Gronenborn, *Biochemistry* **30**, 2316 (1991).
8. J. P. Priestle, H. P. Schär, M. G. Grütter, *Proc. Natl. Acad. Sci. U.S.A.* **86**, 9667 (1989).
9. B. C. Finzel *et al.*, *J. Mol. Biol.* **209**, 779 (1989).
10. B. Veerapandian *et al.*, *Proteins* **12**, 10 (1992).
11. The data used for the joint refinement comprised NMR observations, consisting of 2,780 experimental distance restraints and 390 experimental dihedral restraints (*7*) and 10,429 x-ray reflections extending to 2.0 Å resolution (*10*). Three rounds of simulated annealing with slow cooling (*6*), followed by minimization and restrained temperature factor refinement, which were performed at resolution shells of 2.8, 2.5, and 2.0 Å, caused the *R* value [$R = \Sigma_h|F_0(\mathbf{h}) - F_c(\mathbf{h})|/\Sigma_h\mathbf{F}_0(\mathbf{h})$, where $F_0(\mathbf{h})$ and $F_c(\mathbf{h})$ are the observed and calculated structure factors, respectively] to decrease from the initial value of 0.45 to 0.228 for all of the data to 2.0 Å. Finally, several rounds of minimization at 2.0 Å resolution with the more restrictive PROLSQ (*5*)–like geometry parameters brought the *R* value down to 0.214. Only the six water molecules for which NMR observations could be made (*7*) were included in the model throughout the refinement. In order to monitor the effect of combining the NMR observations with the x-ray data, a conventional crystallographic simulated annealing refinement, starting from the NMR model 6I1B, was performed in parallel to the joint refinement and along the same scheme, yielding an *R* value of 0.216 (model NONOE). In order to calculate the free *R* value of the joint refinement (JR) and the 4I1B models, a cycle of simulated annealing at 600 K was performed, leaving out 10% of the reflections selected at random as described in (*13*). The free *R* values obtained were 0.254 and 0.286 for the JR and 4I1B models, respectively.
12. M. Nilges, G. M. Clore, A. M. Gronenborn, *FEBS Lett.* **229**, 317 (1988).
13. A. T. Brünger, *Nature* **355**, 472 (1992).
14. A. Wlodawer and W. A. Hendrickson, *Acta Crystallogr.* **A38**, 239 (1982).
15. The observation that the 31 to 36 loop in the ensemble of NMR structures does not overlap with the x-ray structures and that this difference stems from a rigid-body hinge movement about residues 31 and 36, indicates that the position adopted in the ensemble of NMR structures probably arise from the nonbonded potential term in the target function (in this case solely a quartic van der Waals repulsion term).
16. A. T. Brünger *et al.*, *Science* **235**, 1049 (1987); W. Braun, O. Epp, K. Wuthrich, R. Huber, *J. Mol. Biol.* **206**, 669 (1989); E. T. Baldwin *et al.*, *Proc. Natl. Acad. Sci. U.S.A.* **88**, 502 (1991).
17. C. Chothia, *J. Mol. Biol.* **105**, 1 (1976).
18. Abbreviations for the amino acid residues are: A, Ala; C, Cys; D, Asp; E, Glu; F, Phe; G, Gly; H, His; I, Ile; K, Lys; L, Leu; M, Met; N, Asn; P, Pro; Q, Gln; R, Arg; S, Ser; T, Thr; V, Val; W, Trp; and Y, Tyr.
19. T. N. Bhat and G. H. Cohen, *J. Appl. Crystallogr.* **17**, 244 (1984).


20. Supported by The AIDS Targeted Anti-Viral Program of the Office of the Director of National Institutes of Health (G.M.C., D.R.D., and A.M.G.). The coordinates of the IL-1β model derived by the joint x-ray–NMR refinement will be deposited in the Brookhaven Protein Data Bank.

5 May 1992; accepted 23 June 1992


# A Critical Role for Conserved Residues in the Cleft of HLA-A2 in Presentation of a Nonapeptide to T Cells


France Latron, Laszlo Pazmany, Joanna Morrison, Robert Moots, Mark A. Saper,* Andrew McMichael, Jack L. Strominger



**The peptide binding cleft of the class I human histocompatibility antigen, HLA-A2, contains conserved amino acid residues clustered in the two ends of the cleft in pockets A and F as well as polymorphic residues. The function of two conserved tyrosines in the A pocket was investigated by mutating them to phenylalanines and of a conserved tyrosine and threonine in the F pocket by mutating them to phenylalanine and valine, respectively. Presentation of influenza virus peptides and of intact virus to cytolytic T lymphocytes (CTLs) was then examined. The magnitude of the reduction seen by the mutation of the two tyrosines in the A pocket suggests that hydrogen bonds involving them have a critical function in the binding of the $NH_2$-terminal $NH_3^+$ of the peptide nonamer and possibly of all bound peptide nonamers. In contrast, the mutations in the F pocket had no effect on CTL recognition.**


The class I and class II glycoproteins encoded in the major histocompatibility complex (MHC) of all vertebrates examined have a central role in immune recognition; they present peptides derived from foreign antigens to the T cell receptor complex on the effector cells of the immune system. These molecules are extremely polymorphic, which leads to the rejection of allogeneic or xenogeneic grafts. The elucidation of the crystal structures of two class I human molecules, HLA-A2 and HLA-